Modeling Transmembrane Transport through Cell Membrane Wounds Created by Acoustic Cavitation

Vladimir Zarnitsyn,* Christina A. Rostad,† and Mark R. Prausnitz*†
*School of Chemical and Biomolecular Engineering, and †Wallace H. Coulter Department of Biomedical Engineering, Georgia Institute of Technology, Atlanta, Georgia

ABSTRACT Cells exposed to acoustic cavitation and other mechanical stresses can be transiently permeabilized to permit intracellular uptake of molecules, including drugs, proteins, and genes. Microscopic imaging and other studies suggest that intracellular loading occurs through plasma membrane wounds of submicrometer radius that reseal over time through the aggregation and fusion of lipid vesicles trafficked to the wound site. The goal of this study was to 1), determine the size of membrane wounds as a function of time after in vitro sonication of DU145 prostate cancer cells under conditions that caused extensive acoustic cavitation; and 2), theoretically model transport processes leading to intracellular loading. Our overall hypothesis was that intracellular loading is governed by passive diffusion through porous membrane wounds of up to 300-nm radius containing pores that permit entry of molecules up to at least 28-nm radius over a timescale of minutes. Experimental measurements showed intracellular loading of molecules with radii from 0.6 to 28 nm, where most loading occurred after sonication over a timescale up to minutes and where smaller molecules were taken up to a greater extent and over a longer timescale than larger molecules. Theoretical modeling predicted that membrane wounds would have a 300-nm radius initially and then would shrink, with a half life of 20 to 50 s. Uptake was shown to occur predominantly by diffusion and the increasing levels of uptake with decreasing molecular size was explained primarily by differences in molecular diffusivity and, for the largest molecule, geometrical hindrance within the wound. Mathematical modeling was simplified, because transport through porous wounds of possibly complex internal nanostructure was governed largely by transport at the edge of the wound, and depended only weakly on the size, number, and distribution of nanopores within the wound under the conditions relevant to this study. Overall, this study developed a theoretical framework for analysis of transmembrane transport through cell membrane wounds and thereby provided quantitative estimates of their size and lifetime.

INTRODUCTION

The study of many intracellular processes and therapeutic interventions on the cellular level often requires delivery of molecules, such as proteins, fluorescent markers, DNA, and RNA, into animal cells. However, intracellular delivery of most hydrophilic molecules is difficult, because animal cells are enclosed by a plasma membrane composed of lipids assembled in a bilayer structure, which creates a formidable barrier for hydrophilic molecules, including water (1).

Over the past few decades, a number of chemical and physical methods have been developed to bypass this membrane barrier. Chemical methods are typically based on associating the molecule with amphiphilic molecules that form a hydrophobic complex with less negative (or more positive) charge (2,3). Using specific formulations, depending on the type of molecule being delivered, this facilitates intracellular transport, generally by active endocytic processes.

Physical methods mostly rely on the transient disruption of plasma membrane structure and thus may be applied to the delivery of many hydrophilic molecules often without the need for protocols customized for each type of molecule. A commonly used physical method is electroporation, in which a microsecond- to millisecond-long electric field pulse causes the stochastic formation of small hydrophilic pores in the plasma membrane with a radius of 1–10 nm (4). These pores are metastable and have a typical lifetime from milliseconds to seconds. Drug and gene delivery during electroporation may be further enhanced by osmotic swelling of cells (5). Other physical methods include application of shear forces using various mechanical tools (6,7), and direct intracellular insertion of a micropipette (8). Mechanically created wounds in the plasma membrane may have dimensions on the micrometer scale, but can still be resealed by cells using active repair processes (9).

Recently, acoustic cavitation has stimulated interest as a method of intracellular delivery for laboratory and future clinical applications (10). Application of high-pressure ultrasound is able to generate, oscillate, and, in some cases, implode gas bubbles in liquid media such as water (11). Upon implosion, collapsing bubbles locally generate pressures up to 10^4 bar and temperatures >1000 K (12). These cavitational oscillations and implosions have been shown to drive intracellular uptake of a number of different molecules by a mechanism believed to involve plasma membrane wounds created in cells within an estimated distance of 10–100 μm from a collapsing bubble by the resulting shock waves and induced shear stress on the membrane surface (13).

Submitted February 26, 2008, and accepted for publication July 1, 2008.

Address reprint request to Dr. Mark Prausnitz, School of Chemical and Biomolecular Engineering, Georgia Institute of Technology, Atlanta, GA 30332-0100. Tel.: 404-894-5135; Fax: 404-894-2291; E-mail: prausnitz@gatech.edu.

Editor: Jason M. Haugh.

0006-3495/08/11/4124/15 $2.00

doi: 10.1529/biophysj.108.131664

Of particular interest for medical applications, ultrasound has been focused noninvasively on cells and tissues in vitro and in vivo to increase intracellular delivery of drugs, proteins, and DNA for transfection (14). In some cases, stabilized microbubbles have been added to nucleate cavitation and further target the effects of ultrasound at sites of bubble localization or binding (15). It has been shown that molecules with a radius up to tens of nanometers are taken up by cells exposed to acoustic cavitation (16). Studies of uptake dynamics showed that the plasma membrane can remain permeable for seconds to minutes after exposure to cavitation (17,18).

Experimental and theoretical studies suggest that intracellular delivery caused by acoustic cavitation is enabled by the formation of wounds in the plasma membrane (18). These breaches in membrane integrity provide a low-resistance pathway for transport into the cell. Membrane effects have been assessed by measuring the extent and time dependence of uptake of fluorescent markers and by microscopic imaging of cells. Several microscopy observations suggest that cavitation facilitates transport through creation of micrometer-size wounds (i.e., holes) on the cell's surface.

Repair of these wounds has been shown to be different from the spontaneous closure of metastable membrane pores created by electroporation (17). The resealing of large wounds created by mechanical impact requires recruitment of intracellular vesicles to the site of disruption so that their lipid material can be used for patching, and the process is ATP-dependent. It is hypothesized that initially these wounds are large holes corresponding to a single pore of equal size to the wound, which may have an understructure of cytoskeleton with high porosity. Over time, the wound is believed to repair by the aggregation and fusion of lipid vesicles trafficked to the wound site, which probably decreases porosity and pore size over time. This mechanism is similar to resealing processes to repair membrane patches damaged by micropipette insertion into a cell (19).

Although a number of experimental studies indicate that intracellular uptake of molecules is mediated by a wound in the plasma membrane that is resealed over time, the structure and dynamics of this wound are poorly understood. Because it is difficult to visualize such processes, this study carried out a theoretical analysis of wound transport and resealing dynamics guided by experimental measurements.

We first sought to determine the overall wound size as a function of time. Because the wound is expected to have a complex and dynamic porous nanostructure within the wound area, we next developed a theoretical approach to model this complexity in the absence of sufficient data to fully characterize it. We expect a complex nanostructure within the wound, because it is well known that cells are tightly packed with macromolecules, organelles, cytoskeleton, and other structures that should provide sieving effects at the nanometer level (1); because the resealing process appears to involve a disorderly self-assembly of lipid structures that eventually form a continuous membrane barrier; and because experimental data have shown selective transport over time as a function of molecular size (17). To explain the observed molecular sieving, we treated the wound area as a porous region that shrinks from its edges while possibly being patched all over its surface until it finally disappears over time. We supported this theoretical development with experimental measurements of intracellular concentration as a function of molecular size and time after sonication. The size of uptake molecules provided information about the size of nanopores within wounds, whereas the time dependence of intracellular concentration provided information about the size of the wound on the membrane surface.

We finally used the resulting theoretical model to predict wound dynamics in terms of their structure and transport properties over time. The work was guided by the hypothesis that intracellular loading is governed by passive diffusion through porous membrane wounds of up to 300-nm radius containing pores that permit entry of molecules up to at least 28-nm radius over a timescale of minutes.

EXPERIMENTAL METHODS

Cell sample preparation

Cell culture and preparation were performed as described previously (20). In brief, human prostate cancer cells (DU145, item no. HTB-81, American Type Culture Collection, Manassas, VA) were cultured as monolayers in a humidified atmosphere of 95% air and 5% CO_2 at 37°C in RPMI-1640 media supplemented with 100 μg/ml penicillin-streptomycin (Cellgro, Mediatech, Herndon, VA) and 10% (v/v) heat-inactivated fetal bovine serum (Atlanta Biologicals, Atlanta, GA). Cells were harvested by trypsin/EDTA (Cellgro) digestion, washed, and resuspended in pure RPMI. The DU145 cell line was used because these cells have been extensively studied in the context of intracellular uptake by acoustic cavitation (16,17,20–23) and are a widely used model for prostate cancer (24).

Before exposure, samples were prepared at a cell concentration of 10^6 cells/ml and Optison concentration of 1.7% v/v ($\sim 1.1 \times 10^7$ bubbles/ml). Optison (Mallinckrodt, St. Louis, MO) is a suspension of perfluorocarbon gas bubbles stabilized with denatured human albumin that were used as nuclei to promote cavitation activity.

Fluorescent molecules

Cell-impermeant, green fluorescent molecules used to quantify molecular uptake into viable cells are listed in Table 1, along with their size and diffusivity. Calcein and dextrans were chosen as biologically inert molecules that generally do not bind to internal cellular structures or organelles. To study the time course of intracellular uptake, 4 μL of a solution of one of the fluorescent molecules in phosphate-buffered saline (PBS; CellGro) was added to 400 μL of a cell suspension either 15 s before sonication or at times 1 s, 15 s, 30 s, 45 s, 60 s, 90 s, 120 s, 240 s, 480 s, or 900 s after sonication at the concentration needed to reach the extracellular concentration listed in Table 1.

Ultrasound apparatus

The ultrasound apparatus has been described previously (22). In brief, an immersible, focused, piezoceramic transducer (H-101, Sonic Concepts, Woodinville, WA) supplied with a matching resistance network allowing production of sound at 1.1 MHz was used as the ultrasound source. The

TABLE 1 Fluorescent molecules used for the intracellular loading study

Fluorescent molecule	Molecular mass (kDa)	D (cm^2/s)*	r_{Stokes} (nm)†	c_0 (μM)
Calcein	0.6	3.6×10^{-6}	0.6	10
Dextran-4	4	1.5×10^{-6}	1.4	100
Dextran-20	20	9.4×10^{-6}	2.3	10
Dextran-150	150	2.4×10^{-7}	8.9	2.5
Dextran-500	500	1.4×10^{-7}	15	1
Dextran-2000	2000	7.7×10^{-8}	28	0.1

*Diffusion coefficient determined in water at 25°C (37).
†The Stokes radius was calculated using the formula $r = kT/(6\pi\eta D)$, where k is Boltzman's constant, T is the absolute temperature, η is the viscosity, and D is the diffusion coefficient.

transducer had a diameter of 70 mm, a 52-mm focal length, and a 1.5-mm focal width at half amplitude (−6 dB).

A sinusoidal waveform was produced by two programmable waveform generators (DS345, Stanford Research Instruments, Sunnyvale, CA; and 33120A, Agilent, Austin, TX) used in conjunction to control pulse length, frequency, and peak-to-peak voltage. The sinusoidal waveform was then amplified by a RF broadband power amplifier (3100LA, Electronic Navigation Industries, Rochester, NY) and passed to the transducer.

The transducer was housed in a polycarbonate tank (30.5 × 29 × 37 cm) containing ~26 L of deionized, distilled, and partially degassed water at room temperature (22–23°C). A 5-cm-thick acoustic absorber (SC-501 Acoustic Rubber, Sonic Concepts) was mounted opposite the transducer to minimize standing wave formation. A three-axis micropositioning system (10 μm resolution, Velmex, Bloomfield, NY) was mounted on top of the tank to position samples and a hydrophone, discussed below, at desired locations in the tank.

To map and calibrate the acoustic field produced by the transducer versus the peak-to-peak voltage signal provided by the function generator, a PVDF membrane hydrophone (MHA200A, NTR Systems, Seattle, WA) was used to measure spatial-peak-temporal-peak negative pressure.

Experimental protocol

Samples were prepared in chambers constructed from the bulb of a polyethylene transfer pipet, as described previously (21). The dimensions of the approximately cylindrical sample chamber were 1.4 cm in height and 0.6 cm in diameter.

A sample solution was slowly aliquoted via a 3-ml syringe (Becton Dickinson, Franklin Lakes, NJ) with a 22-gauge needle (Perkin Elmer, Foster City, CA) into a sample chamber. A metal rod was immediately inserted into the open end of the sample chamber and then attached to the three-axis positioning system.

The sample location was ~1 cm and 0.5 cm out of the ultrasound's focus toward the transducer for 1.1 and 3.1 MHz, respectively. These out-of-focus locations had a broader acoustic beam than at the focus, ~10.4 and 2.4 mm wide at half-amplitude (−6 dB) for 1.1 and 3.1 MHz, respectively. This broader acoustic beam was favorable, allowing a more uniform acoustic exposure across the sample than at the focal point location.

Ultrasound was applied to a sample using a series of 300 pulses at a pulse length of 1 ms, 10% duty cycle (i.e., 100 pulses per second), peak-to-peak pressure of 2 MPa, and frequency of 1.1 MHz. After ultrasound exposure, samples were transferred into 1.5-ml microcentrifuge tubes (Eppendorf, Brinkman, Westbury, NY), and cells were then allowed to ''recover'' for 15 min at room temperature, which is the time determined necessary for cells to reseal themselves (17). As described above, either before sonication or at a specified time during the recovery period, a solution with one of the fluorescent molecules was added to the cell suspension. After this recovery period, samples were washed with PBS and centrifuged (800 × g, 3 min, Eppendorf 5415C, Brinkman, Westbury, NY) three times to remove supernatant with extracellular molecules. The resulting cell pellets were resuspended in 200 μL of PBS containing 0.2 μL of propidium iodide (P-1304, 0.1 mg/ml, Molecular Probes, Eugene, OR), which is a viability marker that stains nonviable cells with red fluorescence.

Quantification of bioeffects

Flow cytometry was used to determine on a cell-by-cell basis the levels of molecular uptake, i.e., the number of cells with significantly increased green fluorescence due to intracellular uptake of calcein or dextran, and the loss of cell viability, i.e., the number of cells with significantly increase red fluorescence due to penetration of propidium iodide. A BD LSR benchtop flow cytometer (BD Biosciences, San Jose, CA) was used to measure the fluorescence of cells with calcein/dextran uptake (530/28-nm bandpass filter) and to distinguish viable from nonviable cells by the fluorescence of propidium iodide (670-nm bandpass filter). A total of 10,000 viable cells were analyzed by flow cytometry in each sample. In a typical sample, the viable cell population represented ~60% of the treated cells. The level of fluorescence required to differentiate uptake from nonuptake cells was chosen such that 99% of cells in the nontreated sample have fluorescence below this level. The percent of cells with fluorescence above this level in treated samples was used to quantify uptake in terms of uptake percent.

We also ran flow cytometry with the addition of microbeads with fluorescence calibrated in FITC units that allowed us to convert relative units of fluorescence into the absolute number of molecules taken up by cells. We measured the fluorescence of test molecules relative to FITC units with the use of a fluorimeter to be able to calculate the number of molecules taken up by cells and—dividing by cell volume—their intracellular concentration, as described previously (16). We observed that even when molecules were added long after ultrasound exposure, cell fluorescence was somewhat elevated in a time-independent manner. We interpreted this as nonspecific staining of cell membranes affected by ultrasound, and not as intracellular uptake. We therefore subtracted this background fluorescence from uptake calculations.

To determine the viability in treated samples, cells were counted and normalized on the basis of analyte volume. The analysis time of a sample in the flow cytometer was used as a measure of the volume analyzed because the flow cytometer operated at a constant flow rate. Viability was determined as the ratio of viable cell concentrations in treated and control samples. This approach accounts for intact nonviable cells that appear as propidium iodide-positive cells in the flow cytometer and for ''lost'' cells destroyed by ultrasound that appear as debris in the flow cytometer (22).

EXPERIMENTAL RESULTS AND THEORETICAL ANALYSIS

It is known that ultrasound generates cavitational bubble activity, which in turn creates transient wounds in the plasma membrane of cells and thereby permits intracellular uptake of molecules (10). This study sought to use theoretical analysis guided by experimental measurements to determine the overall wound size, nanoporous structure within wounds, and wound transport properties as a function of time after exposure to ultrasound during the wound repair process. Our approach involves three consecutive steps. First, we experimentally measured intracellular uptake of molecules of different sizes (Stokes radius (r_{Stokes}) 0.6–28 nm) added at different times after sonication (0–25 min) to cell suspensions exposed to ultrasound. Second, we coupled these experimental mea-

surements with theoretical analysis to convert uptake data into time-dependent cell membrane permeability. Finally, we determined geometrical properties of the wounded membrane from permeability measurements using equations justified in the Appendix.

Experimental findings

As a function of time after sonication, we measured the fraction of cells able to take up molecules of various sizes. As shown in Fig. 1 *A*, 24% of cells were able to take up the smallest molecule, calcein ($r_{Stokes} = 0.6$ nm), when it was added before or immediately after sonication. The dextrans ($r_{Stokes} = 1.4$–28 nm) were taken up by 10–25% of cells, in which range the percent of cells with uptake decreased as a function of molecular size (analysis of variance (ANOVA), $p < 0.001$). When molecules were added at later times after sonication, the fraction of cells with uptake decreased with increasing time for all molecules tested (ANOVA, $p < 0.001$) and reached zero uptake by 900 s after sonication in all cases.

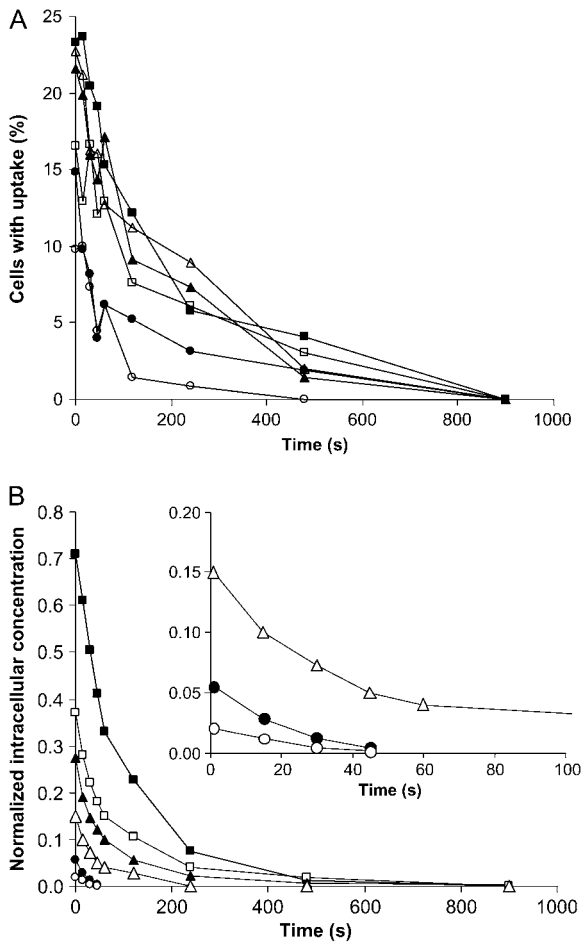

FIGURE 1 Experimental measurements of intracellular loading with fluorescent molecules as a function of time and molecule size. (*A*) Percent of cells with uptake of molecules. (*B*) Intracellular concentration of those molecules among cells with uptake as a function of time elapsed after sonication before each molecule was added. Inset shows an expanded view of the data at short times. The uptake molecules are calcein (■), dextran-4 (□), dextran-20 (▲), dextran-150 (△), dextran-500 (●), and dextran-2000 (○). Data points represent the average of $n = 3$ measurements. For clarity of presentation, error bars are not shown, but the average standard error of the mean is 6% in *A* and 7% in *B*.

Although it is of interest to note that only a fraction of cells take up molecules, which can be explained by the spatial and temporal heterogeneity of cavitation activity and bubble collapse (23), those cells, and their associated transport processes, are the focus of this study. We therefore carried out additional analysis including only those cells with uptake (i.e., ''wounded'' cells) and measured the intracellular concentration as a function of time and molecule size. As shown in Fig. 1 *B*, the intracellular concentration was a strong function of both time and molecule size (two-way ANOVA, $p < 0.001$). The smallest molecule, calcein, was delivered into cells at a normalized concentration of up to 0.79 (i.e., the intracellular concentration was 79% of the extracellular concentration, indicating a near equilibrium), whereas the largest molecule, dextran-2000, was delivered into cells at a normalized concentration of only up to 0.02. The intracellular concentration decayed in an approximately exponential fashion as the molecules were added at later times. Calcein uptake was seen up to 900 s after sonication, whereas uptake of dextran-2000 became negligible after just 45 s.

It was of specific interest to compare uptake among cells initially exposed to the molecules before sonication to cells initially exposed to the molecules immediately after sonication. This comparison allows us to assess the possible role of convective forces and other phenomena caused directly by the mechanical activity of cavitating bubbles present only during sonication. As shown in Fig. 2 *A*, the fraction of cells with uptake of molecules added before and immediately after sonication were statistically indistinguishable for all of the molecules tested (two-way ANOVA, $p = 0.07$). As shown in Fig. 2 *B*, the number of molecules/cell was also statistically the same for molecules added before and immediately after sonication (two-way ANOVA, $p = 0.11$). This indicates that transport during cavitation and other effects of ultrasound present during sonication was not needed for intracellular delivery.

These experimental results set the stage for theoretical analysis. Some timescales are established: little transport occurs during sonication, the timescale for uptake of large molecules is on the order of 1 min after sonication and the timescale for uptake of small molecules is on the order of 10 min after sonication. It is, however, unknown to what extent the observed differences in uptake are caused by differences in diffusivity and how much should be attributed to the effects of size sieving at the wounded membrane. It is also unknown how the wounded area and nanopore structure change over time. These questions can be answered by modeling.

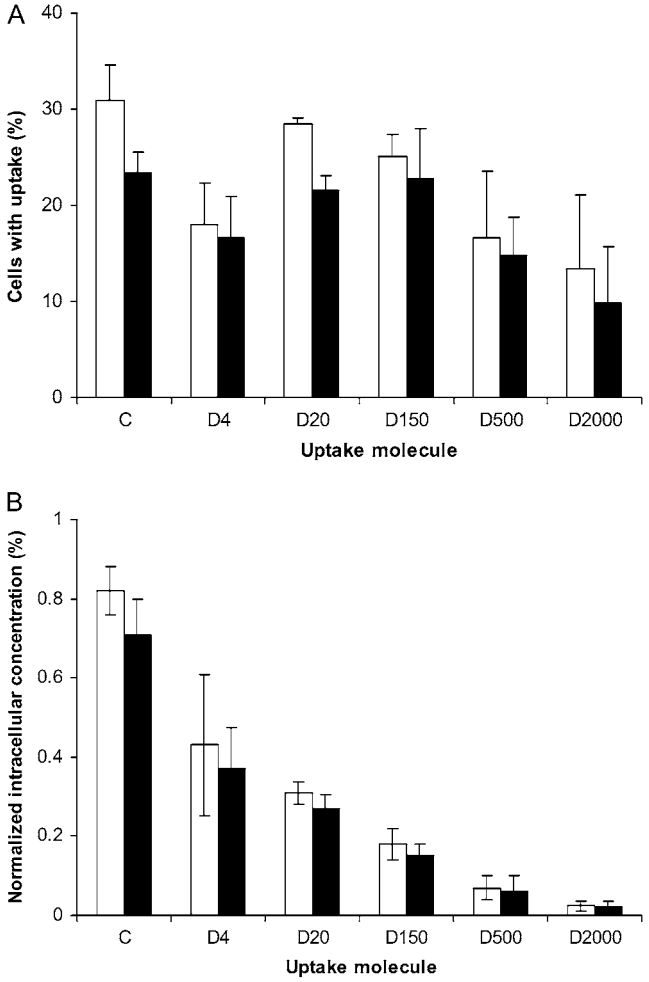

FIGURE 2 Comparison of (*A*) the percent of cells with molecular uptake and (*B*) the inctracellular concentrations when molecules were added within 15 s before sonication (*white bars*) or within 1 s after sonication (*black bars*) for different molecules: calcein (*C*), dextran-4 (*D4*), dextran-20 (*D20*), dextran-150 (*D150*), dextran-500 (*D500*), and dextran-2000 (*D2000*). Data come from Fig. 1 and represent the average of $n = 3$ measurements. Error bars show the standard error of the mean. Statistical analysis using a two-way ANOVA indicated no significant difference between uptake of molecules added before versus those added after sonication ($p = 0.067$).

Theoretical analysis

Role of nondiffusive intracellular uptake

Intracellular uptake could occur by a number of mechanisms. We hypothesize that diffusion is the predominant mechanism, because the timescales for other modes of transport are too short. We quantitatively assess this hypothesis in the following paragraphs. Although active transport processes, such as endocytosis, could be imagined to play a role, this possibility has already been ruled out by previous work (17). We therefore focus our analysis on physical transport mechanisms that do not rely on cellular transport machinery.

The formation of a plasma membrane wound may lead to water fluxes in and out of the cell due to osmotic imbalance. In this experiment, cells were in isotonic solution, so the gradient of osmotic pressure should be small. Moreover, the restoration of osmotic balance should be fast, which can be estimated as the characteristic time of water diffusion inside the cell (t_{os}) through a wound of characteristic size, R (estimated at 300 nm, as a representative value; see below)

$$t_{os} = \frac{R_{cell}^3}{D_w R} \approx \frac{10^{-15} m^3}{10^{-9}\frac{m^2}{s} 10^{-6} m} \approx 1\,s, \qquad (1)$$

where R_{cell} is the cell radius and D_w is water diffusivity in cells. In this analysis, $t_{os} \approx Q/J$, where Q is the total amount of redistributed water, which has an upper limit estimated as the total cell volume (V) multiplied by water concentration (c), to yield $Q \leq cV$; and J is the transport rate through the opening of radius R, which is estimated as $J \approx D_w cR$ (discussed in more detail in the Appendix). As a result $t_{os} \leq V/(D_w R)$, which leads to the above equation. This scaling analysis shows that even if osmotic effects take place, they are transient and disappear 1 s after membrane wounding.

Another possible cause of convective transport into a cell could be electrical or thermal gradients. However, we did not apply electric fields and did not heat the system. Nonetheless, the wound could cause discharge of the transmembrane potential with a characteristic time (t_U) of

$$t_U = \frac{C_{cell}}{\sigma R} \approx \frac{10^{-11} F}{1\,\Omega^{-1} m^{-1} 10^{-7} m} \approx 10^{-4} s, \qquad (2)$$

where C_{cell} is the cell capacitance and σ is the extracellular conductivity. In this analysis, cell capacitance was estimated as $C_{cell} = \varepsilon_{mem}\varepsilon_0(S_{cell}/h)$, where ε_{mem} is the membrane dielectric constant (~4–8), ε_0 is the dielectric constant of vacuum (8.85×10^{-12} F/m), S_{cell} is the cell surface area (~1000 μm^2), and h is the membrane thickness (~5 nm). This scaling analysis shows that any electrical discharge is a transient process that disappears with a characteristic time of 10^{-4} s after wounding.

A third source of convection may be caused directly by cavitation bubble mechanics during ultrasound treatment. The characteristic time of bubble implosion and hydrodynamic fluxes during cavitation may be estimated as $\sim 1/f = 10^{-6}$ s, where f is the ultrasound frequency. Thus, once again, this convective process is very short-lived compared to the timescale over which intracellular transport occurs experimentally, as shown in Fig. 2. We therefore conclude that any convective component of transport does not play a significant role except for the first 1 s after cell wounding and that the only mechanism governing the transport on the scale of seconds and minutes is passive diffusion through long-lived wounds in the plasma membrane.

For completeness, it is also worth noting that convective mixing occurred upon addition of molecules to the cell suspensions at various times after sonication. However, the timescale of this mixing was short (~1 s) and its intensity much weaker than the violent mixing generated during ultrasound treatment.

Intracellular uptake by diffusion

Analysis of intracellular uptake by diffusion is controlled by the overall wound size and the size and distribution of pores within the wound. These geometrical parameters are shown in the model of a wounded cell presented in Fig. 3. In this figure, the extracellular space is characterized by diffusivity, D, and concentration of molecules, c_0; the intracellular space is characterized by diffusivity, D_{in}, and concentration, c_{in}; and the plasma membrane has a thickness h and contains a wounded region with a time-dependent radius, $R(t)$, composed of randomly located nanopores with radius r through which molecular transport can occur.

There are, however, too many unknowns to fully characterize the time-dependent geometry of the wound and its distribution of nanopores. We therefore analyzed the transport problem to reduce the number of independent parameters. The analysis in the Appendix shows that if certain assumptions are valid, we can adequately characterize the wound and its complex nanostructure with just the overall wound radius.

A brief explanation of the underlying physics of this effect is as follows. Our first assumption is that the radius of the wound (i.e., ~100 nm) is much greater than its thickness (i.e., plasma membrane thickness ~5 nm). Our second assumption is that there is a ''sufficiently large'' number of nanopores in the wound. By combining these assumptions, we find that transport to and from the wound surface is rate-limiting, and transport through the wound is relatively fast, because diffusion through the 5-nm-thick nanopores should be fast relative to diffusion between the bulk solution and the wound area. In this way, only the overall wound radius matters, because this is the length scale that governs the rate of diffusion to and from the wound edge. A detailed quantitative justification for this analysis is provided in the Appendix.

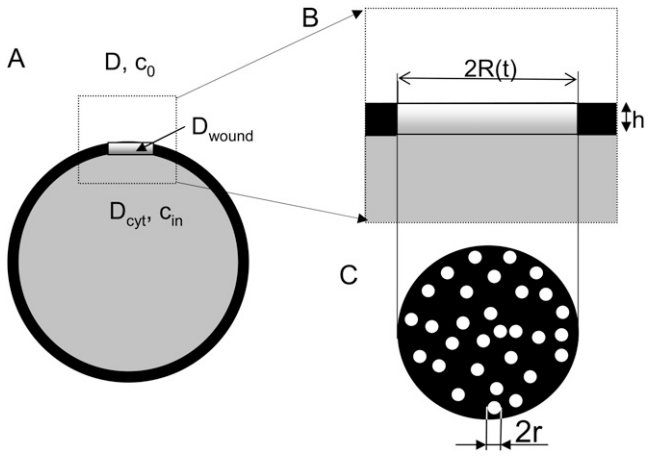

FIGURE 3 Model of a plasma membrane wound, in which a simplified geometry of a cell with a plasma membrane wound (*A*) has diffusion coefficients D, D_{cyt}, and D_{wound} in the extracellular space, intracellular space, and within the wound, respectively, extracellular concentration far from the cell surface c_0, and concentration inside the cell c_{in}. An enlarged cross-sectional view of the wounded area (*B*) depicts a wound with radius $R(t)$ and thickness h. The view of the wounded area from above (*C*) depicts nanopores of radii r randomly located within the wound.

Given this analysis, we can apply a mass balance to the simplified case of transport through a single circular pore with radius equal to the wound size:

$$V\frac{dc_{\alpha i,in}}{dt} = J_\alpha, \tag{3}$$

where the subscript α identifies the molecule, the subscript i identifies the time of molecule addition to the external media, and J is the time-dependent rate of transport into the cell.

We can continue this analysis by analogy with Eq. A16 in the Appendix, and by considering that diffusion into a cell is a three-part process involving 1), diffusion to the wound, 2), diffusion across the cell membrane within the wound, and 3), diffusion away from the wound in the cytosol:

$$J_\alpha = \frac{c_{\alpha 0}(t) - c_{\alpha,in}(t)}{\dfrac{h}{D_{\alpha,pore}S_{pore}} + \dfrac{1}{4D_\alpha R} + \dfrac{1}{4D_{\alpha,in}R}} = VP_\alpha(t)(c_{\alpha 0}(t) - c_{\alpha,in}(t)), \tag{4}$$

where V is the cell volume, h is the membrane thickness, R is the wound radius, S_{pore} is the total area of porated surface (total area of all nanopores), $D_{\alpha,pore}$ is the diffusivity of molecule α inside a nanopore, D_α is the diffusivity of molecule α in water, $D_{\alpha,in}$ is the diffusivity of molecule α inside the cell, t is time, and $P_\alpha(t)$ is a transport coefficient introduced for convenience of subsequent analysis. In this equation, the first term in the denominator represents the diffusion resistance within nanopores, and the second and third terms represent the resistances to diffusion to and from the wound surface outside and inside the cell, respectively.

The wound area may be estimated as $S_{pore} \approx R^2$, assuming a high density of nanopores. Diffusivity in the pore, $D_{\alpha,pore}$, lies between the extra- and intracellular diffusivities, assuming no hindrance. Any actual possible hindrance was accounted for by reducing the effective calculated wound size, S_{pore}. As a result, the ratios of the first term in the denominator of Eq. 4 to the other two are of the order of h/R. Consistent with our previous analysis, this first term may be neglected if we are interested in transport through large wounds with $R \gg h$. It is worth noting that this situation is quite different from the typical situation during electroporation, where pore radius is similar or even smaller than membrane thickness and therefore diffusional resistances to, within, and from electropores are all of the same order of magnitude (4).

Equation 4 was derived for intracellular concentration independent of time. However, if the characteristic time of wound radius changes is significantly longer than the characteristic time of diffusion relaxation, t_D, in the wound entrance/exit zones ($t_D \approx R^2/D_\alpha$), then we can apply Eqs. 3 and 4 to the time-dependent intracellular concentration as well (a pseudo-steady-state solution, as discussed by Cussler (25). Because the diffusion relaxation time is ~30 μs for calcein and ~1 ms for dextran-2000 (see Table 1 for diffusivity values) for a wound of $R \approx 100$ nm, and the characteristic

experimental time for wound resealing is tens of seconds (Fig. 1), it is accurate to integrate Eqs. 3 and 4 (stationary diffusion) with nonstationary $R(t)$ and hence nonstationary $P_\alpha(t)$. See also Table 2.

Diffusion coefficients

To apply transport equations (Eqs. 3 and 4), we need to identify intracellular and extracellular diffusivities of the transported molecules. Extracellular diffusivities are listed in Table 1. To determine intracellular diffusivities, we estimated the ratio of intracellular to extracellular diffusivity for all molecules to be 0.27 based on experimental measurements in the literature (26). We believe that this estimate is appropriate because, for example, diffusivity in the cytoplasm relative to that in water (D_{in}/D) was 0.27 ± 0.01 in fibroblasts and 0.26 ± 0.01 in MDCK cells, and this ratio was independent of FITC-dextran and ficoll size over the range of gyration radii from 4 to 30 nm (27).

Calculation of cell volume

We also need to determine cell volume, V, because it affects the characteristic time of cell equilibrium loading. Confocal images of cells loaded with fluorescent molecules after sonication showed that although small calcein molecules were distributed throughout the cell, larger dextran molecules filled the cytosol but were excluded from the nucleus (16). This indicates that ultrasound opened the plasma membrane, but did not affect the nuclear membrane, which is normally permeable to small molecules like calcein, but impermeable to large dextrans. To determine appropriate cell volumes, we used light microscopy to measure cell and nucleus radii as 8 ± 1 and 5 ± 1 μm, respectively. Assuming a spherical cell and nucleus shape, we estimate cell volume as 2000 μm^3, nucleus volume as 400 μm^3, and cytoplasm volume as 1600 μm^3.

TABLE 2 Definition of symbols

Symbol	Meaning
C_{cell}	Cell capacitance
c_0	Extracellular concentration
c_{in}	Intracellular concentration
D	Extracellular diffusivity
D_{in}	Intracellular diffusivity
D_w	Diffusivity of water
D_{pore}	Diffusivity inside a nanopore
F	Ultrasound frequency
H	Membrane thickness
i	Subscript identifying time of addition
J	Transport rate into the cell
P	Transport coefficient (introduced in Eq. 4)
R	Wound radius
R_{cell}	Cell radius
r	Nanopore radius
S_{cell}	Cell surface area
S_{pore}	Total area of porated surface
T	Time
t_i	Time of addition of fluorescent molecules
t_{os}	Characteristic time of osmosis
t_U	Characteristic time of cell discharge
V	Cell volume
α	Subscript identifying the molecule
γ	Coefficient in denominator of Brown equation (discussed in Eq. A12)
ε_0	Dielectric constant of vacuum
ε_{mem}	Dielectric constant of membrane
σ	Extracellular conductivity

Determination of time-dependent wound radius

The goal of the next section is to derive equations that use intracellular uptake measurements to calculate the transport coefficient $P_\alpha(t)$ and thereby determine wound radius R as a function of time.

First, we specify the initial condition of zero intracellular concentration before the addition of molecules to the cell suspension at time t_i

$$c_{\alpha,in}(t < t_i) = 0. \tag{5}$$

We next identify that the extracellular concentration $c_{\alpha 0}(t)$ abruptly changes from zero to the value $c_{\alpha 0}$ at t_i, which can be expressed as a step function

$$c_{\alpha 0}(t) = \begin{cases} 0, & t < t_i \\ c_{\alpha 0}, & t \geq t_i \end{cases}. \tag{6}$$

The solution of Eq. 3 with the boundary conditions of Eqs. 5 and 6 is

$$c_{\alpha,in}(t) = c_{\alpha 0} \times \left[1 - \exp\left(-\int_{t_i}^{t} P_\alpha(t)dt\right)\right], \tag{7}$$

and thus,

$$c_{\alpha,in}(t = \infty) = c_{\alpha 0} \times \left[1 - \exp\left(-\int_{t_i}^{\infty} P_\alpha(t)dt\right)\right]. \tag{8}$$

Equation 8 indicates that the transport coefficient, P_α, is related to the final intracellular molecule concentration, $c_{\alpha,in}(t = \infty)$, which has been measured experimentally (Fig. 1 *B*). Recognizing this, Eq. 8 can be transformed as

$$\int_{t_i}^{\infty} P_\alpha(t) = \ln\left(\frac{1}{1 - \dfrac{c_{\alpha,in}(t = \infty)}{c_{\alpha 0}}}\right). \tag{9}$$

Because the final intracellular concentration has been measured experimentally for a series of times, t_i, we can use experimental values for two subsequent times, t_i and t_{i+1} to derive

$$\int_{t_i}^{t_{i+1}} P_\alpha(t)dt = \ln\left(\frac{1 - \dfrac{c_{\alpha i}(t = \infty)}{c_{\alpha 0}}}{1 - \dfrac{c_{\alpha(i+1)}(t = \infty)}{c_{\alpha 0}}}\right). \tag{10}$$

If we assume that the transport coefficient remains constant over the period of time between t_i and t_{i+1}, which can be expressed as

$$\int_{t_i}^{t_{i+1}} P_\alpha(t)dt \approx P_\alpha(t_i) * (t_{i+1} - t_i). \quad (11)$$

Then we can finally derive the equation

$$P_\alpha(t_i) = \frac{1}{(t_{i+1} - t_i)} \ln\left(\frac{1 - \frac{c_{\alpha i}(t=\infty)}{c_{\alpha 0}}}{1 - \frac{c_{\alpha(i+1)}(t=\infty)}{c_{\alpha 0}}}\right). \quad (12)$$

Substituting Eq. 12 into Eq. 4 and neglecting the first term in the denominator of Eq. 4 yields the final expression used to determine time-dependent wound radius R as a function of intracellular uptake measurements $c_{\alpha,\text{in}}(t = \infty)$

$$R(t_i) \approx \frac{V(D_\alpha + D_{\alpha,\text{in}})}{4D_\alpha D_{\alpha,\text{in}}(t_{i+1} - t_i)} \ln\left(\frac{1 - \frac{c_{\alpha i,\text{in}}(t=\infty)}{c_{\alpha 0}}}{1 - \frac{c_{\alpha(i+1),\text{in}}(t=\infty)}{c_{\alpha 0}}}\right). \quad (13)$$

Using Eq. 13 in combination with data shown in Fig. 1 *B*, we were able to estimate wound size as a function of time independently for each of the test molecules (Fig. 4). In this analysis, wound radius R was the only fitted parameter. Estimated wound radii for all studied molecules followed the same trend of an almost exponential decay, with a half life between 20 s (dextran-2000) and 55 s (calcein). Wounds were completely resealed by 900 s after sonication, at which time the calcein transport through it was negligible. It is notable that the estimates of wound radius and resealing kinetics according to the data from each of the six different test molecules are almost the same, which supports the accuracy of model predictions.

Because individual data points are difficult to read on Fig. 4, wound sizes determined from transport of the different molecules immediately after sonication are shown on Fig. 5 *A*. All five molecules ranging in size from 0.6 nm (calcein) to 15 nm (dextran-500) transported through wounds with a radius, R, of ~300 nm that contained nanopores of at least 15-nm radius. It is interesting to note that although experimental uptake levels were strong functions of molecular size (Fig. 1), after mathematical treatment these five molecules all independently predict the same wound radii. This suggests that the differences in uptake levels can be explained predominantly by the different diffusivities of these molecules rather than a complex distribution of nanopore sizes.

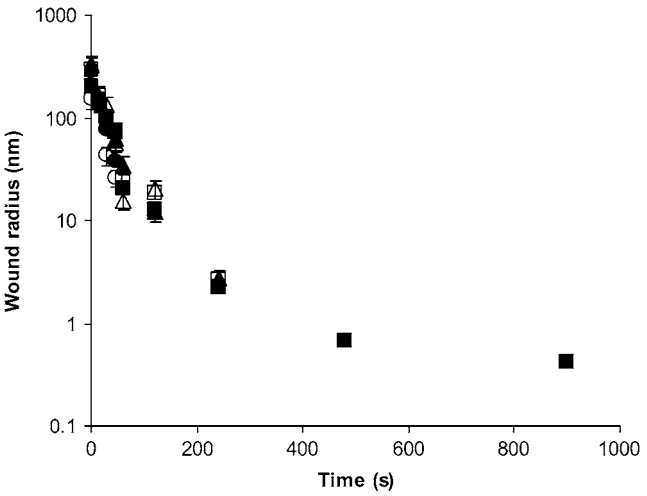

FIGURE 4 Calculated wound radius as a function of time and molecule being transported: calcein (■), dextran-4 (□), dextran-20 (▲), dextran-150 (△), dextran-500 (●), and dextran-2000 (○). Wound radii were calculated based on Eq. 13. Data points represent the average of $n = 3$ calculations (each from independent experimental data) with error bars showing the standard deviation.

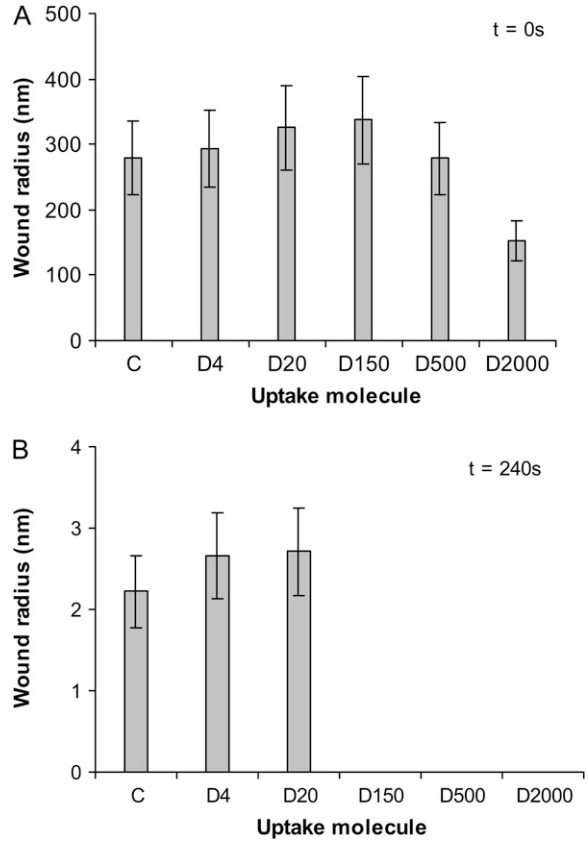

FIGURE 5 Calculated wound radius at $t = 0$ s (*A*) and $t = 240$ s (*B*) as a function of the molecule being transported: calcein (*C*), dextran-4 (*D4*), dextran-20 (*D20*), dextran-150 (*D150*), dextran-500 (*D500*), and dextran-2000 (*D2000*). (*A*) Wound radii calculated from uptake of molecules smaller than dextran-2000 are statistically indistinguishable (ANOVA, $p = 0.52$) and equal to ~300 nm. (*B*) Wound radii calculated from uptake of molecules smaller than dextran-150 are statistically indistinguishable (ANOVA, $p = 0.15$) and equal to ~2.5 nm. Data represent the average of $n = 3$ calculations (each from independent experimental data in Fig. 1 *B*), with error bars showing the standard deviation.

As shown in Fig. 5 *A*, the largest molecule, measuring 28-nm in radius (dextran-2000), accessed a smaller wound area with a radius of ~150 nm. This suggests that roughly three-fourths of the area of the 300-nm radius wound had nanopores between 15 nm and 28 nm in effective radius, and the remaining one-fourth of the wound area (corresponding to an effective radius of 150 nm) had nanopores >28 nm. This sieving effect could be explained by hindrance of dextran-2000 diffusion, possibly due to interaction with the cytoskeleton. Alternatively, the anomalous behavior of dextran-2000 could be an error due to an overestimate of the intracellular diffusivity of dextran-2000, which would predict an artificially small wound radius, or an incorrect measurement of intracellular concentrations of dextran-2000, which were often near the noise limit of the flow cytometry data.

At later times, wounds became significantly smaller. Fig. 5 *B* shows wound radii at 4 min after sonication. The data from the three smallest molecules (with molecular radii of 0.6 nm to 2.3 nm) all indicate wound radii of ~2.5 nm. The other three larger molecules (with molecular radii of 8.9–28 nm) were not taken up by cells at that time, which is also consistent with a wound of radius 2.5 nm.

DISCUSSION

The main goals of this article were to study the dynamics of intracellular loading after plasma membrane disruption by acoustic cavitation, to identify parameters of the wound geometry that control molecule transport, and to quantitatively estimate these parameters by coupling theoretical analysis with experimental data.

Experimental data showed that molecules as large as 28 nm were able to enter cells after sonication, but those rates of intracellular loading decreased with increasing time and molecular size (Fig. 1). By developing a physical and mathematical description of intracellular loading through resealing membranes, we estimated effective wound size as a function of time (Figs. 4 and 5). Effective wound radius was determined to be as large as 150–300 nm for all test molecules immediately after sonication. This size is consistent with previous microscopic images of ultrasonically wounded cells (17,18). The wound resealed by decreasing its effective radius with a characteristic half-life of 20–50 s, depending on molecule size. Within 4 min, wounds decreased in radius to 2.5 nm and did not allow molecules >2.5 nm inside the cell. This suggests that the initial wound is large, with an internal structure composed of a complex collection of nanopores, but at the end of the resealing process there appears to be a single hole of molecular dimensions. We believe this represents the first quantitative estimate of the dynamics of wound size after exposure to acoustic cavitation.

This study considered cell loading with molecules over a broad range of sizes from 0.6 to 28 nm. Lacking knowledge of the detailed nanostructure of pore distribution within wounds, our model was only able to consider hindrance to transport through the wounds as a step function, i.e., molecules were transported through wounds with a constant diffusivity as long as the wound size was greater than the molecule size and were unable to transport through wounds smaller than the molecule size. Actual possible hindrance due to transport through small nanopores within a larger wound were accounted for by reducing the effective wound size calculated. Using this approach, the model predicted the same wound sizes at the initial time point for all but the largest molecule (dextran-2000, with a radius of 28 nm). The effective wound radius for the largest molecule was a factor of 2 smaller, which corresponds to an area that was a factor of 4 smaller, which suggests a hindrance of 0.25.

This analysis suggests that the size of any nanostructured sources of transport hindrance were larger than the second largest molecule (dextran-500, with a radius of 15 nm) and similar in size to the largest molecule. We hypothesize that the source of this hindrance does not come from features of the resealing wound, but instead derives from the cytoskeleton network present immediately below the resealing membrane, which has a spectrin-to-spectrin spacing of the order of 70 nm (28). This barrier could hinder dextran-2000, with a 28-nm radius (i.e., a 56-nm diameter), but not significantly affect transport of dextran-500, with a 15-nm radius, or the other smaller molecules.

Scaling analysis of characteristic times of different plausible modes of intracellular loading indicated that convective loading related to cavitation-associated mixing, osmotic imbalance, and membrane electrical discharge should dissipate over a characteristic time of 1 s or less. However, the experimental data showed that intracellular loading when molecules were added before sonication was statistically indistinguishable from when molecules were added within seconds after sonication. This indicated that intracellular loading that can occur during the subsecond timescale of convective phenomena is not significant and, therefore, passive diffusion through long-lived wounds is the main mechanism of intracellular loading for all of the macromolecules studied.

Our theoretical analysis of the transmembrane flux relied on determining an effective membrane permeability, which would in general depend on the nanostructure of the wound geometry. However, analysis was simplified by modeling the wound as a system of equivalent circular pores randomly distributed in the wound area, as described in the Appendix. The analysis was further simplified by recognizing that the only parameter that influences transport through the wound is wound radius as long as the following three conditions are met: 1), molecules are much smaller than the wound size and smaller than the associated nanopores; 2), membrane thickness is much smaller than wound size; and 3), wound surface is sufficiently porated, where the sufficiency depends on the pore radii (see Appendix and Fig. 7). It is not intuitively obvious that the porosity of the wounded surface plays only a small role. However, in the example of a nanopore radius/

wound radius ratio of 1:100, a 10-fold increase in the porosity from 10% to 100% only increases the diffusive flux through the wound by 11% (Appendix, Fig. 7 *B*). The exact location of the pores in the wound plays an even smaller role, as long as they are uniformly distributed. As a result, experimental data on intracellular loading permitted us to calculate the wound size without having to characterize the possibly complex nanostructure within the wound.

These findings indicate that wounds created by acoustic cavitation are up to 100 times larger and 100 times longer-lived than pores created by electroporation, which are on the order of 1–10 nm and have a lifetime of up to seconds (4). These differences are probably due to the different mechanisms by which these membrane defects are created and reseal. In contrast, wounds created by other mechanical methods, including fluid mechanical shear and direct mechanical trauma (19), appear experimentally similar in terms of size, lifetime, and mechanism of repair (17). We therefore hypothesize that the analysis presented in this study may be more broadly applicable to cellular wounds generated by other mechanical methods. Mechanical wounding of cells and their associated resealing are important processes that are believed to occur naturally not only in cells in vitro, but within organized tissues in the human body. Wounding may be associated with normal physiology, disease, and medical intervention for drug/gene delivery or other procedures (14,18).

These finding can also be used to improve future applications of ultrasound for intracellular delivery of drugs, genes, and other compounds in the laboratory or the clinic. The finding that plasma membrane wounds are initially on the order of 100 nm and that reduced uptake with increasing molecular size can mostly be explained simply by reduced diffusivity through wounds of the same effective size (i.e., no hindrance) suggests that very large molecules and complexes may be delivered into cells, although the apparent hindrance observed by the 2000-kDa dextran may indicate an upper limit. The finding that the rate-limiting step to intracellular delivery is transport to and from the wound suggests that more aggressive cavitation that makes larger wounds may be a less beneficial strategy (given the likely associated increase in cell death) compared to methods that increase transport within the boundary layer surrounding the cell and within the cytoplasm. The finding that intracellular transport is predominantly by diffusion suggests that uptake could be increased by the addition of convective, electrophoretic, or other driving forces.

The main conclusions of this study are that experimental measurements showed intracellular loading with molecules ranging from 0.6 to 28 nm in size over a timescale of minutes. A theoretical model was developed to analyze these data and was used to predict, for the first time, the effective plasma membrane wound size created by acoustic cavitation. These wounds were found to be up to 300 nm in radius immediately after sonication, to decay in size with a half-life of 20–50 s, and to reseal over characteristic times of minutes, depending on the molecule being transported. Scaling analysis showed that the major mechanism of intracellular loading was passive diffusion. Additional analysis showed that transmembrane flux was dependent primarily on overall wound size and depended only weakly on the possibly complex porous nanostructure within the wound. Overall, this work supported the hypothesis that intracellular loading is governed by passive diffusion through porous membrane wounds of up to 300-nm radius containing pores that permit entry of molecules up to at least 28-nm radius over a timescale of minutes.

APPENDIX

Acoustic cavitation creates wounds on the cell surface with an unknown shape and a possibly complex structure due to remnants of cellular structures and cytoskeleton. Modeling of transport through such a wound requires knowledge of the detailed geometry of possible nanostructures within the wound. However, such information does not exist. We therefore hypothesize that the permeability of a porous membrane wound can be approximated by the permeability of a single hole with a radius equal to the effective wound radius and is generally independent of the size, shape, density, and distribution of nanopores within the wound area. We expect this hypothesis to be true, because scaling analysis, discussed above, associated with Eq. 4 indicates that transport into a cell is limited by diffusion to and from the wound and not diffusion through the wound itself. We test this hypothesis on a model wound represented as a set of nanopores randomly located on a circular wound patch.

Mathematical formulation of the problem

The steady-state problem of passive diffusion through a perforated membrane that is symmetrically located between two compartments can be mathematically formulated in terms of Laplace's equation with mixed boundary conditions (29). Our overall goal is to compare the permeability of an empty wound (i.e., one big hole) with porous wounds having nanopores of various size, shape, density, and distribution. To keep the extent of analysis manageable, we did not vary many variables at once and considered only simplified geometries for the problem. Because the mathematical formulation of the problem has no analytical solution, we numerically calculated steady-state mass transfer rates through randomly porated membranes of finite thickness. The heterogeneity of poration was modeled by randomly positioning different numbers of pores of the same radius, r, on the nodes of a regular honeycomb mesh within a circular area of radius R. To capture the general trends of each solution, we ran at least three simulations for every set of parameters.

Infinitesimally thin membrane

Analytical solutions for mixed boundary value problem

Our analysis begins with the simplification of an infinitesimally thin membrane, for which there are exact analytical solutions for some geometries. Although we ultimately must solve the problem with a membrane of finite thickness, there are no exact analytical solutions in this case, which complicates analysis. An initial assumption of an infinitesimally thin membrane is justified, because the cell membrane is thin (5 nm) compared to characteristic initial wound radii (~300 nm).

Using the Laplace equation with mixed boundary values, we first model stationary transport through a single circular hole of radius R in an infinitesimally thin membrane. If the concentration is given far above (c_0) and far below ($c = 0$) the horizontal plane of the membrane, then the steady-state flux, J, through the hole is (29)

$$J = 2DRc_0 \tag{A1}$$

and the flux density distribution around the hole area is (29)

$$j(\rho) = \frac{2Dc_0}{\sqrt{R^2 - \rho^2}}, \tag{A2}$$

where ρ is the distance from the center of the hole to the point of flux measurements. Eq. A2 indicates that the flux density increases infinitely near the edges of the hole and that the central area of the hole is not very important for transport through it.

We can further check the importance of the edge area for transport by comparing to transport through annular holes. In this case, the central part of inner radius, R_{in}, of a hole of outer radius R is closed to transport. The solution for this problem may be adapted from a similar electrostatic solution of Cooke, as described by Sneddon (29). In Table 3, we provide the ratio of the flux through an annular hole to the flux through a circular hole, where both have an outer radius R, and the inner radius, R_{in}, of the annulus is varied. These calculations show that mass transfer through the annulus is surprisingly insensitive to the size of the central part of the hole. The last line of Table 3 indicates that only 4% of the area near the edge of a hole is enough to provide two-thirds of the transport through all of the hole. This suggests that transport through a membrane wound may similarly depend largely on the mass transfer along its edges.

Because a wound may be made up of many closely spaced nanopores within the wound, it is also important to understand the effect of neighboring holes on each other. The above analysis suggests that any changes near the edges of a hole are very important for transport properties, such that closely located pores may strongly compete for transport and screen each other.

To investigate this influence in greater detail, we considered the problem of two identical circular holes of radius R as a function of hole-to-hole spacing, which has been solved analytically by Kobayashi, as described by Sneddon (29). When the holes' edges touch, the flux through each hole is only 75% of the flux through an individual hole of the same radius R. When the center-to-center separation of the holes is $10R$, the flux through each hole reaches 94% of the flux through a single hole. This indicates that as pore density increases among closely spaces pores, the relative contribution of further increasing pore density has diminishing effects. This has implications for possible porous networks within cell wounds of presumably high porosity.

We conclude from this analysis that 1), transport through the edge areas of holes accounts for the majority of mass transfer; and 2), closely located holes screen mass transfer through each other. These two observations show that mass transfer through a system of closely spaced pores is not simply the sum of transport through each of those pores in isolation.

Numerical methods

Our next goal was to model transport through a system of pores of rather general geometry using numerical simulations for randomly generated systems of pores located within a finite wound area to develop statistically significant functional relationships between the number of pores, N, their radii, r, and the wound radius, R, as input parameters and mass transfer through this system as the output parameter. We studied the problem by varying the number of individual pores from 1 to 2500, the ratio of pore radius r to wound radius R from 0.0025 to 0.1, and, as discussed in the next section, membrane thickness from 0 to $40r$. Because we were interested in the statistical properties of the solution, we repeated calculations three times for each set of parameters. However, solution of the Laplace equation with mixed boundary values using numerical methods such as finite-element methods or boundary integral methods demands intensive calculations. Application of conventional methods to fully perform the proposed numerical simulations would take years of computer time.

TABLE 3 Steady-state flux through annular area

R/R_{in}	$S_{annulus}/S_{circle}$	$J_{annulus}/J_{circle}$
2.0	75%	0.981
1.5	55.6%	0.9494
1.25	36.0%	0.8976
1.2	30.6%	0.8776
1.125	21.0%	0.8326
1.091	16.0%	0.8011
1.021	4.1%	0.6667

To make this problem more manageable, we found that Fabrikant developed an approximate numerical approach to this problem that allows computing exact upper and lower bounds of the mass transfer coefficient for a system of arbitrary circular pores located on a membrane (30). Mathematically this approach consists of three steps. The first step is the derivation of exact integral equations (Eq. A5). The second step is approximation of the integrals of mutual interactions for each pair of pores. They are integrals over the circular pore's interior and may be estimated as the value of the function at some point, $\bar{y}$, in the circle multiplied by the area of the circle according to the average value theorem (Eq. A6). The theorem does not provide the exact position of the point $\bar{y}$ within each circle. The mutual screening of pores increases when the distance between the center of one circle to some point $\bar{y}$ in the other circle decreases and vice versa. This gives a way to estimate the upper and lower limits for mass transfer through the system of pores. The lower limit for mass transfer may be calculated if we propose that for each pair of pores the mutual screening is the maximum possible. Conversely, the upper bound for mass transfer may be calculated if we propose that for each pair of pores the mutual screening is minimal. The third step is the solution of the system of linear equations (Eq. A11) with an order equal to the number of pores. The numerical execution of these operations is several orders of magnitude faster than standard methods due to the need for just one element for each pore.

We have first used this approach for a membrane of zero thickness and a system of pores represented in Fig. 3 with a uniform diffusivity everywhere D, intracellular concentration, c_{in}, equal to 0, extracellular concentration, c_0, greater than zero, and multiple circular pores (with area designated as S_i in the following formulation) in the horizontal thin plane.

Application of Fabrikant's method for this case starts with the Newton-potential integral solution for the Neumann problem of the Laplace equation (31), which states that in the case of a flat boundary, the concentration everywhere $c(x)$ may be found by integrating over the membrane

$$c(x) = \frac{1}{2\pi}\int_{S_{mem}} \int \frac{\left(\frac{\partial c}{\partial n}\right)_y}{\rho(x,y)} dS_y, \tag{A3}$$

where $(\partial c/\partial n)_y$ is the normal derivative of the concentration, c, taken at a boundary point, y, and $\rho(x,y)$ is the distance from x to y. In our case, this normal derivative is nonzero only at the pore's surface, because there is no flux or concentration gradient through intact membrane. As a result, we may rewrite Eq. A3 as

$$c(x) = \frac{1}{2\pi}\sum_{n=1}^{N}\int_{S_n} \int \frac{\left(\frac{\partial c}{\partial n}\right)_y}{\rho(x,y)} dS_y, \tag{A4}$$

where S_n is the surface area of the nth pore.

Fabrikant's approach to this equation consists of its integration over the surface of each individual pore with appropriate weighting functions. For example, by integrating it with the weight function f_1 defined below over the surface of the first pore S_1, the following equation results:

$$2\pi\int_{S_1}\int f_1(y)c(y)dS = \left(\int_{S_1}\int \left(\frac{\partial c}{\partial n}\right)_y dS_y + \sum_{n=2}^{N}\int_{S_n}\int w_{1n}(y)\left(\frac{\partial c}{\partial n}\right)_y dS_y\right), \tag{A5}$$

where y is a two-dimensional coordinate on the membrane surface, $c(y)$ is the concentration inside the first pore (equal to $c = (c_{in} + c_0)/2$ due to the symmetry of the problem), and $w_{1n}(y)$ are integral functions given below.

The $f_1(y)$ function is defined as

$$f_1(y) = \frac{1}{\pi^2 r_1} \frac{1}{\sqrt{1 - \dfrac{\rho^2(y, y_1)}{r_1^2}}}, \tag{A6}$$

where y_1 gives the coordinates of the center of the first circle and r_1 is its radius. The function $f_1(y)$ satisfies two integral equations

$$\int_{S_1} \int \frac{f_1(y)}{\rho(y, y')} dS_y = 1, \quad \forall y' \in S_1$$
$$\int_{S_1} \int f_1(y) dS_y = \frac{2r_1}{\pi}, \tag{A7}$$

where $\rho(\mathbf{y},\mathbf{y}')$ is the distance from y to y',

Integrals w_{1n} in Eq. A5 are given by

$$w_{1n}(y') = \int_{S_1} \int \frac{f_1(y)}{\rho(y, y')} dS_y = \frac{2}{\pi} \sin^{-1}\left(\frac{r_1}{\rho(y', y_1)}\right), \tag{A8}$$

where y' is located inside pore S_n, and y_1 is the coordinate of the center of the first pore.

Integrals on the right side on Eq. A5 contain unknown concentration gradients $(\partial c/\partial n)_y$ that may be estimated by the mean value theorem

$$\int_{S_n} \int w_{1n}(y) \left(\frac{\partial c}{\partial n}\right)_y dS_y = w_{1n}(\tilde{y}) \int_{S_n} \int \left(\frac{\partial c}{\partial n}\right)_y dS_y, \tilde{y} \in S_n. \tag{A9}$$

We further take into account that the integral of the concentration gradient in a normal direction over the pore surface S_n is related to the diffusion rate through that surface, J_n:

$$D \int_{S_n} \int \left(\frac{\partial c}{\partial n}\right)_y dS_y = J_n. \tag{A10}$$

Application of this approach to all pores results in the exact system of linear equations (one for each value of j from 1 to N)

$$4Dr_j c_j = \left(J_j + \frac{2}{\pi} \sum_{\substack{n=1 \\ n \neq j}}^{N} J_n \sin^{-1} \frac{r_j}{r_{nj}}\right), \tag{A11}$$

where N is the number of pores; r_n and r_j (n and j vary from 1 to N) are the radii of the nth and jth pores, respectively; J_n and J_j are the transport rates through the nth and jth pores, respectively; r_{nj} is the distance from the center of the nth circle to the point $\tilde{y}$ within the jth circle; and c_j is the concentration inside the jth pore, equal to c. The solution of this system of equations (Eq. A11) provides the transport rate through each individual pore. Total transport rate through the wound area may be found as the sum of individual pore transport rates.

The method in its original description by Fabrikant does not provide a recipe for choosing $\tilde{y}$ and r_{nj}. The strength of the method, however, is that by varying all r_{nj} within their limits ($r_{nj}^0 - r_i < r_{nj} < r_{nj}^0 + r_{i,}$, where r_{nj}^0 is the distance between the centers of pores n and j), one may obtain exact upper and lower limits for the total transport rate. In the majority of cases we studied, the upper and lower approximations were surprisingly close to each other. We compared the smallest, central, and largest possible estimations for calculated fluxes through the system of pores. For each system of randomly distributed pores, we solved the system of equations A11 (j varied from 1 to N) with all r_{nj} taken at their maximal values (for the upper limit of transport), minimal values (for the lower limit for transport), or exactly equal to the distance between the centers of the circular pores (for the central estimate). We found that the variation among these approaches was within 10% (Fig. 6). This consistency may be explained by the fact that the mass transfer is mostly influenced by pores located far from each other due to screening by neighboring pores. For these pores, the difference between the lower and upper bounds of r_{nj} is very small relative to the distance between pores. Overall, this analysis shows that the exact distribution of pores within a wound may have only a weak effect on total mass transport.

Given this weak effect of pore-to-pore spacing, our subsequent simulations used the central approximation for r_{nj} to calculate total transport rate through the system of pores. As an independent validation of Fabrikant's method with the central approximation, we compared the approximate solution with the exact results discussed above for two circular pores (32). It was found that Fabrikant's method gave estimates for the total transport rate within 0.4% of the exact solution for all pore-to-pore distances (i.e., $r \leq r_{nj} < \infty$) and within 0.1% when $r_{nj} \geq 2.4r$.

We next examined the effect of the number and radius of pores in a wound by solving the system of equations A11 for random distributions of circular pores with equal radii r located within a wound area with radius R and varying the number of pores from 1 to 2500 and their relative radius r/R from 0.0025 to 0.1. In this analysis, we considered 1200 different wound/pore geometries with the goal of determining under which conditions the transport rate through a system of pores in a wound approaches the maximum transport rate through an empty hole (i.e., a wound with 100% porosity).

The simulation results from this analysis are shown in Fig. 7 as a function of the number of pores (Fig. 7 *A*), total area of pores (Fig. 7 *B*), and total circumference of pores (Fig. 7 *C*). Fig. 7 *A* shows that as pore size increases, fewer pores are needed to approach the maximum transport rate (e.g., just a few pores of $r/R = 0.1$ suffice). Fig. 7 *B* shows that as pore size decreases, a smaller total pore area (i.e., porosity) is needed to approach the maximum transport rate (e.g., just a few percent porosity for pores of $r/R = 0.0025$ suffice). This observation that a system of many small pores is more permeable than a system of fewer large pores of the same total pore area can be explained by Fig. 7 *C*, which shows that for all numbers and sizes of pores considered, the transport rate generally depends on the total pore

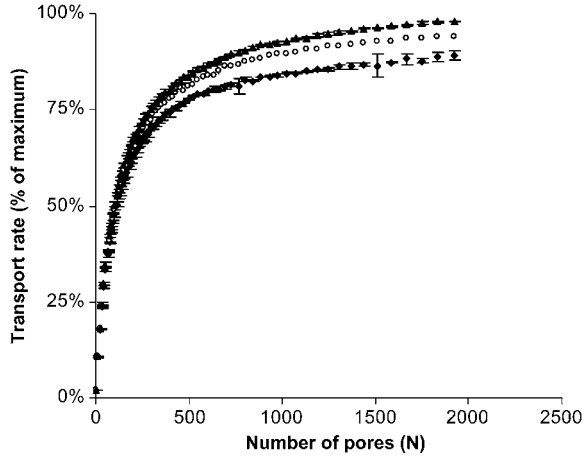

FIGURE 6 Comparison between the lowest (♦), central (○), and highest (▲) estimates of transport rate through a system of pores using numerical calculations by Fabrikant's method (Eq. A11). Pores with radius $r = 0.01R$ were randomly located at the nodes of a hexagonal mesh within a circular wound of radius R. Each point is the average of three simulations with different randomly generated systems of pores. Error bars show the standard deviation.

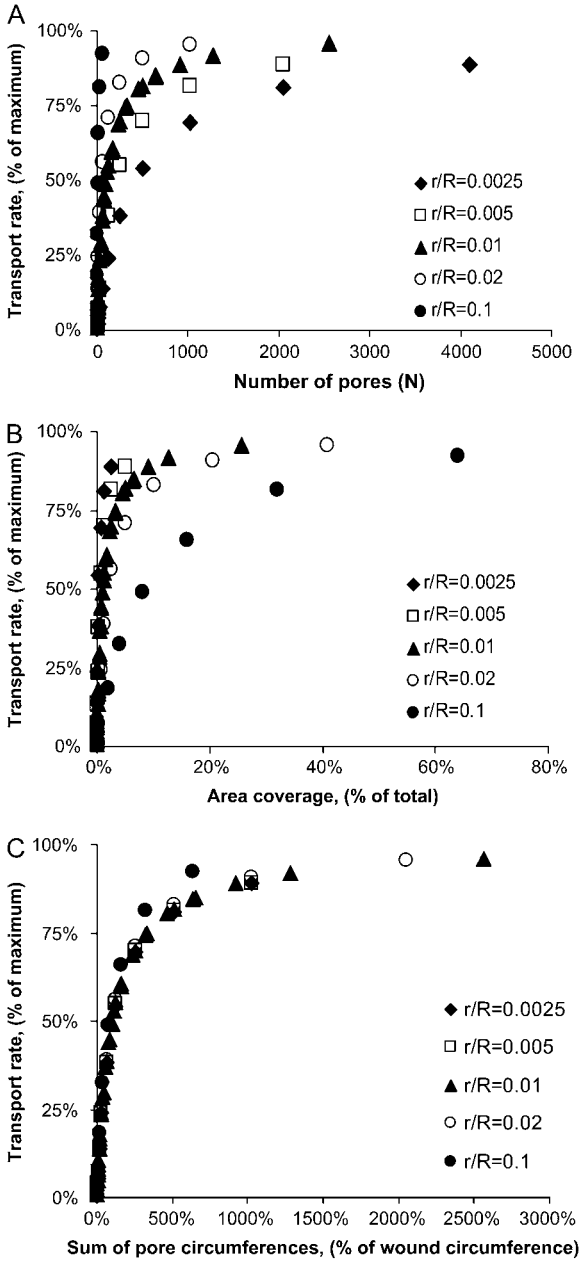

FIGURE 7 Transport rate through a system of pores with radii r/R (varied between 0.0025 and 0.1) randomly located within a wound of radius R as a function of (*A*) the number of pores, (*B*) the total area of the pores expressed as a percent of the wound area (i.e., porosity), and (*C*) the sum of the pore circumferences expressed as a percent of the wound circumference. Transport rate is expressed as the percent of the transport rate through an open hole of radius R in an infinitely thin membrane. Each point is the average of three calculations with different randomly generated systems of pores. For clarity of presentation, error bars are not shown, but the average standard deviation is 1.4%.

circumference. This finding indicates that transport to the pore edges is the limiting step, which is consistent with our previous analysis of transport through annular holes presented in Table 3.

As an aside, we note that the results shown in Fig. 7 are paradoxical. If we construct a system of N pores (where $N \approx 1/r$) of infinitesimally small radius r, the total area will tend to zero ($S \approx Nr^2 \approx r$), whereas the total circumference of the system of pores will be fixed ($\sim$1). Mass transfer through this system is predicted to be significant when considering its total circumference (Fig. 7 *C*), but will be zero when considering its total area (Fig. 7 *B*). This type of relationship between surface area and mass transfer was previously observed in the literature for a one-dimensional electrode problem of complex (fractal) shape (33). However, this effect has limited practical relevance to our problem, because it is impossible to pick pore radii less than the molecular radius and still observe significant mass transfer.

Overall, the results of this numerical analysis indicate that for practical applications, the rate of transport through a system of pores within a wound may be predicted with good accuracy without complete information about the location of the pores. When the ratio of r/R is small, the mass transport rate already approaches its maximum value dictated by the radius of the wound when those pores cover just a few percent of the wound area. This relationship is not sensitive to the number of pores or their particular distribution over the surface. This finding makes the wound radius a useful parameter to characterize mass transfer properties of a system of pores.

Thick membrane

In the previous analysis, we assumed an infinitely thin membrane. Our next goal was to take into account the finite thickness of the membrane. The approximate equation of mass transfer through an open circular area in a thick membrane was proposed by Brown (34) as

$$J = \frac{2Drc_0}{1 + \frac{2h}{\pi r}}, \tag{A12}$$

where h is the membrane thickness and r is the pore radius.

Equation A12 was derived with the assumption that concentration is uniform over the top surface of the pore. Lord Rayleigh argued that this uniform concentration assumption is not always justified and that the term equal to 1 in the denominator of Eq. A12 should be replaced by α, which is a function of the ratio of the membrane thickness, h, to the pore radius, r, and lies within the interval $1 \le \gamma \le 1.049$ (35). Recently the function $\gamma(h/r)$ was calculated numerically and the upper limit of possible values of α was found to be 1.046 (36). Thus, the assumption of uniform concentration ($\gamma = 1$ in denominator) on the pore surface is reasonable within 4.6% accuracy.

We note that the system of equations A11 will be applicable to the thick membrane problem if instead of concentration in the plane of symmetry c_j we use the concentration at the top edges of the thick pores (c_j'). The top edge is located at a distance of $h/2$ from the plane of symmetry through the midpoint of the pore length. The concentration on the top edge of the pore (c_j'), transport rate through it (J_j), and concentration in the middle plane (c_j) are related by the equation

$$J_j = \frac{D\Delta c S_{pore}}{h/2} = 2D\frac{c_j' - c_j}{h}\pi r_j^2. \tag{A13}$$

Replacing c_j and c_n with c_j' and c_n', respectively, in Eq. A11, and combining with Eq. A13, we derive the following system of linear algebraic equations (one equation for each value of j from 1 to n), which represents Eq. A11 updated to account for membrane thickness:

$$4Dr_j c_j = \left(J_j\left(1 + \frac{2h}{\pi r_j}\right) + \frac{2}{\pi}\sum_{\substack{n=1 \\ n\neq j}}^{N} J_n \sin^{-1}\frac{r_j}{r_{nj}} \right). \tag{A14}$$

Although Eq. A14 can be used, we were interested to have a simpler solution and therefore approximated the overall transport rate for the thick membrane (J_h) as the transport rate through two diffusive resistances connected in series. One resistance is the system of pores in an infinitely thin membrane and the other resistance is a tube with a cross section equal to the total area of pores and a length equal to the membrane thickness.

$$J_h = \frac{c_o}{\frac{h}{DS_{pore}} + \frac{c_0}{J_0}}, \quad \text{(A15)}$$

where J_0 is the total transport rate through the system of pores determined by Eq. A11 and S_{pore} is the total area of pores on the wound.

To assess the validity of the simplified approach of Eq. A15, we compared results from Eq. A14 to those from Eq. A15 for a representative system of pores with radius $r = 0.01R$ on a membrane of thickness h that varied from $0.02r$ to $40r$. The simple approximations from Eq. A15 (Fig. 8, *continuous lines*) were in close agreement (i.e., within 3%) with the simulation results from Eq. A14 (Fig. 8, *discrete points*) over the broad range of membrane thicknesses considered. Because cell membrane thickness is approximately 5 nm, setting $h = 2r$ corresponds to a pore radius of 2.5 nm, which is of molecular dimensions and representative of the smallest pore likely to exist for mass transfer. Fig. 8 shows that for this scenario, the finite membrane thickness decreased the transport rate through the pore by <5%. For larger pores, corresponding to smaller values of h/r, the effect of membrane thickness is even smaller.

Further simplification can be achieved if we assume that the wound surface is sufficiently porated and the flux J_0 can be estimated from Eq. A1.

$$J_h = \frac{c_0}{\frac{h}{DS_{pore}} + \frac{1}{2DR}}. \quad \text{(A16)}$$

CONCLUSION

This analysis showed that transport through a system of pores in a membrane wound 1), is governed largely by transport at the edge of a wound; 2), depends weakly on the size, number, and distribution of pores in the wound when r/R is small, even at small porosities, and when r/R approaches unity at large porosities; and 3), depends weakly on membrane thickness for pores of molecular dimensions or larger.

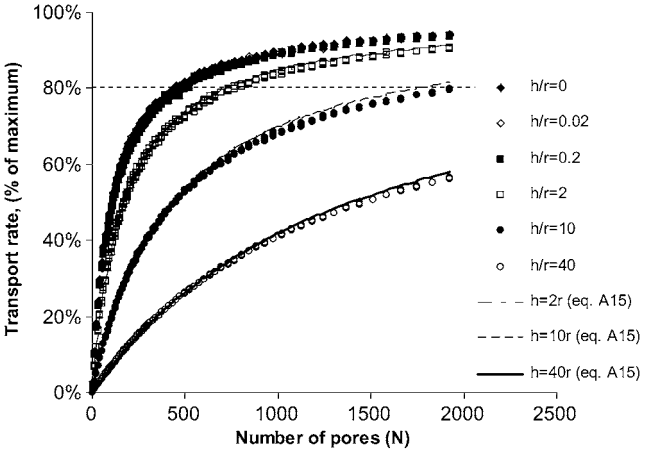

FIGURE 8 Transport rate through a system of pores of radius $r/R = 0.01$ randomly located within a wound of radius R as a function of the number of pores for different membrane thicknesses h/r: 0 (♦), 0.02 (◇), 0.2 (■), 2 (□), 10 (●), and 40 (○). Data points were generated numerically using Eq. A15, and continuous curves were generated analytically using Eq. A14. Transport rate is expressed as the percent of the transport rate through an open hole of radius R in an infinitely thin membrane.

Plasma membrane wounds created by acoustic cavitation are hypothesized initially to be large holes corresponding to a single pore of equal size to the wound, which may have an understructure of cytoskeleton with high porosity. Over time, the wound is believed to repair by the aggregation and fusion of lipid vesicles trafficked to the wound site. This probably decreases porosity and pore size over time. Because the loss of porosity is compensated for by an increase in total pore circumference due to the presence of many small pores, we hypothesize that the detailed characterization of the pore population is still relatively unimportant to determining mass transfer through the wound. As the wound reaches the final stages of closure, it may contain just one or a small number of small pores, but at that point the effective wound size also decreases and the small pore(s) may have a size similar to the wound size and, therefore, a porosity that is large. Thus, we believe that dynamic changes in wound geometry can generally be characterized as having either large pores (relative to wound size) at high porosity or small pores at a range of possible porosities. In each of these scenarios, the assumptions made in our analysis are valid. Given this analysis, we have characterized the transport through porous wounds on the assumption that they have enough pores that transport does not depend on the number or size of individual pores (Fig. 7) and depends only on the size of the porated area, as expressed in Eq. A16. This equation may be easily developed into Eq. 4 to take into account that diffusivity is different inside and outside of a cell.

We thank Johnafel Crow, Daniel Hallow, and Robyn Schlicher for helpful discussions. This work was carried out in the Center for Drug Design, Development and Delivery and the Institute for Bioengineering and Bioscience at Georgia Tech. V.G.Z. designed and analyzed uptake experiments and carried out all theoretical development. C.M.R. carried out and analyzed uptake experiments. M.R.P. helped design and interpret the study and served as the principal investigator.

This work was supported in part by the National Institutes of Health.

REFERENCES

1. Lodish, H., A. Berk, S. L. Zipursky, P. Matsudaira, D. Baltimore, and J. E. Dornell. 2000. Molecular Cell Biology. W.H. Freeman, New York.
2. Langer, R. 1990. New methods of drug delivery. *Science*. 249:1527–1533.
3. Li, X., and B. R. Jasti. 2006. Design of controlled release drug delivery systems. McGraw-Hill, New York.
4. Weaver, J. C., and Y. Chizmadzhev. 1996. Theory of electroporation: a review. *Bioelectrochem. Bioenerg.* 41:135–160.
5. Golzio, M., M. P. Mora, C. Raynaud, C. Delteil, J. Teissie, and M. P. Rols. 1998. Control by osmotic pressure of voltage-induced permeabilization and gene transfer in mammalian cells. *Biophys. J.* 74:3015–3022.
6. Fechheimer, M., J. F. Boylan, S. Parker, J. E. Sisken, G. L. Patel, and S. G. Zimmer. 1987. Transfection of mammalian cells with plasmid DNA by scrape loading and sonication loading. *Proc. Natl. Acad. Sci. USA*. 84:8463–8467.
7. Zarnitsyn, V. G., J. M. Meacham, M. J. Varady, C. Hao, F. L. Degertekin, and A. G. Fedorov. 2007. Electrosonic ejector microarray for drug and gene delivery. *Biomed. Microdevices*. 10:299–308.

8. Kobayashi, N., J. D. Rivas-Carrillo, A. Soto-Gutierrez, T. Fukazawa, Y. Chen, N. Navarro-Alvarez, and N. Tanaka. 2005. Gene delivery to embryonic stem cells. *Birth Defects Res. C Embryo Today*. 75: 10–18.

9. McNeil, P. L., S. S. Vogel, K. Miyake, and M. Terasaki. 2000. Patching plasma membrane disruptions with cytoplasmic membrane. *J. Cell Sci.* 113:1891–1902.

10. Paliwal, S., and S. Mitragotri. 2006. Ultrasound-induced cavitation: applications in drug and gene delivery. *Expert Opin. Drug Deliv*. 3:713–726.

11. Leighton, T. G. 1994. The Acoustic Bubble. Academic Press, London.

12. Pecha, R., and B. Gompf. 2000. Microimplosions: cavitation collapse and shock wave emission on a nanosecond time scale. *Phys. Rev. Lett.* 84:1328–1330.

13. Sundaram, J., B. R. Mellein, and S. Mitragotri. 2003. An experimental and theoretical analysis of ultrasound-induced permeabilization of cell membranes. *Biophys. J.* 84:3087–3101.

14. Mehier-Humbert, S., and R. H. Guy. 2005. Physical methods for gene transfer: improving the kinetics of gene delivery into cells. *Adv. Drug Deliv. Rev.* 57:733–753.

15. Unger, E. C., T. O. Matsunaga, T. McCreery, P. Schumann, R. Sweitzer, and R. Quigley. 2002. Therapeutic applications of microbubbles. *Eur. J. Radiol.* 42:160–168.

16. Guzman, H. R., D. X. Nguyen, A. J. McNamara, and M. R. Prausnitz. 2002. Equilibrium loading of cells with macromolecules by ultrasound: effects of molecular size and acoustic energy. *J. Pharm. Sci.* 91:1693–1701.

17. Schlicher, R. K., H. Radhakrishna, T. P. Tolentino, R. P. Apkarian, V. Zarnitsyn, and M. R. Prausnitz. 2006. Mechanism of intracellular delivery by acoustic cavitation. *Ultrasound Med. Biol.* 32:915–924.

18. Mehier-Humbert, S., T. Bettinger, F. Yan, and R. H. Guy. 2005. Plasma membrane poration induced by ultrasound exposure: implication for drug delivery. *J. Control. Release.* 104:213–222.

19. McNeil, P. L., and R. A. Steinhardt. 2003. Plasma membrane disruption: repair, prevention, adaptation. *Annu. Rev. Cell Dev. Biol.* 19:697–731.

20. Guzman, H. R., D. X. Nguyen, S. Khan, and M. R. Prausnitz. 2001. Ultrasound-mediated disruption of cell membranes. I. Quantification of molecular uptake and cell viability. *J. Acoust. Soc. Am.* 110:588–596.

21. Zarnitsyn, V. G., and M. R. Prausnitz. 2004. Physical parameters influencing optimization of ultrasound-mediated DNA transfection. *Ultrasound Med. Biol.* 30:527–538.

22. Hallow, D. M., A. D. Mahajan, T. E. McCutchen, and M. R. Prausnitz. 2006. Measurement and correlation of acoustic cavitation with cellular bioeffects. *Ultrasound Med. Biol.* 32:1111–1122.

23. Guzman, H. R., D. X. Nguyen, S. Khan, and M. R. Prausnitz. 2001. Ultrasound-mediated disruption of cell membranes. II. Heterogeneous effects on cells. *J. Acoust. Soc. Am.* 110:597–606.

24. Webber, M. M., D. Bello, and S. Quader. 1996. Immortalized and tumorigenic adult human prostatic epithelial cell lines: characteristics and applications. Part I. Cell markers and immortalized nontumorigenic cell lines. *Prostate.* 29:386–394.

25. Cussler, E. L. 2008. Diffusion: Mass Ttransfer in Fluid Systems. Cambridge University Press, New York.

26. Verkman, A. S. 2002. Solute and macromolecule diffusion in cellular aqueous compartments. *Trends Biochem. Sci.* 27:27–33.

27. Seksek, O., J. Biwersi, and A. S. Verkman. 1997. Translational diffusion of macromolecule-sized solutes in cytoplasm and nucleus. *J. Cell Biol.* 138:131–142.

28. Sackmann, E. 1994. Intracellular and extracellular macromolecular networks: physics and biological function. *Macromol. Chem. Phys.* 195:7–28.

29. Sneddon, I. N. 1966. Mixed Boundary Value Problems in Potential Theory. John Willy & Sons, New York.

30. Fabrikant, V. I. 1987. Diffusion through perforated membrane. *J. Appl. Phys.* 61:813–816.

31. Vladimirov, V. S. 1984. Equations of Mathematical Physics. Mir, Moscow.

32. Kristiansson, S., S. P. Kagganti, F. Ingvarson, and K. O. Jeppson. 2005. A comparison of the exact and an approximate solution for the resistance between two coplanar circular discs. *Solid-State Electron.* 49:275–277.

33. Phillips, C., A. Ben-Richou, A. Ambari, and A. Fedorov. 2003. Catalyst surface at a fractal of cost: a quest for optimal catalyst loading. *Chem. Eng. Sci.* 58:2403–2408.

34. Brown, H. T., and F. Escombe. 1900. Static diffusion of gases and liquids in relation to the assimilation of carbon and translocation in plants. *Philos. Transact. R. Soc. Lond. B.* 193:223–291.

35. Rayleigh, J. W. S., and R. B. Lindsay. 1945. The Theory of Sound. Dover, New York.

36. Brunn, P. O., V. I. Fabrikant, and T. S. Sankar. 1984. Diffusion through membranes: effect of a nonzero membrane thickness. *Q. J. Mech. Appl. Math.* 37:311–324.

37. Aldrich. 2007. Handbook of Fine Chemicals (catalog). Sigma-Aldrich, St. Louis, MO.